Graphene-Based Nanoplatelets: A New Risk to the Respiratory System as a Consequence of Their Unusual Aerodynamic Properties

Anja Schinwald,[†] Fiona A. Murphy,[†] Alan Jones,[‡] William MacNee,[†] and Ken Donaldson[†,*]

[†]Centre for Inflammation Research, Queen's Medical Research Institute, MRC/University of Edinburgh, 47 Little France Crescent, Edinburgh EH16 4TJ U.K. and [‡]Institute of Occupational Medicine, Research Avenue North, Riccarton, Edinburgh EH14 4AP U.K.

Graphene, a two-dimensional (2D) crystalline material comprising a single layer of carbon atoms tightly packed into a honeycomb lattice has recently been identified[1] and has attracted substantial scientific interest due to its unique intrinsic properties. However, the novel platelet-like shape has drawn our attention to the toxicology of these emerging materials. Unintentional occupational or environmental exposure to graphene-based materials during manufacturing or intentional exposure *via* biomedical applications are likely with their increasing development and use. Thus far, the information on the inhalation toxicity of graphene nanoplatelets (GP) or platelet-shaped particles in general is very limited.[2] Nanoplatelets may pose an unusual risk to the lungs and the pleural space because of their aerodynamic properties. Deposition in the respiratory tract is determined by the aerodynamic diameter (Dae) which is defined as the diameter of a sphere of unit density with the same terminal settling velocity as the particle itself.[3] The respiratory or pulmonary fraction denotes the size fraction of particles, <5 μm Dae, that deposit beyond the ciliated airways where alveolar macrophages are the main clearance mechanism, and is considered to pose the highest risk in health terms. Sanchez *et al.* recently calculated the deposition fraction of graphene nanoplatelets with different lateral dimensions ranging from 0.001 to 100 μm in the nasopharyngeal, tracheobronchial, and alveolar region either moving along or perpendicular to the polar axis.[2] This theoretical calculation revealed that there would be substantial deposition of such nanoplatelets throughout the respiratory tract. Normally alveolar macrophages only encounter compact particles elutriated

ABSTRACT

Graphene is a new nanomaterial with unusual and useful physical and chemical properties. However, in the form of nanoplatelets this new, emerging material could pose unusual risks to the respiratory system after inhalation exposure. The graphene-based nanoplatelets used in this study are commercially available and consist of several sheets of graphene (few-layer graphene). We first derived the respirability of graphene nanoplatelets (GP) from the basic principles of the aerodynamic behavior of plate-shaped particles which allowed us to calculate their aerodynamic diameter. This showed that the nanoplatelets, which were up to 25 μm in diameter, were respirable and so would deposit beyond the ciliated airways following inhalation. We therefore utilized models of pharyngeal aspiration and direct intrapleural installation of GP, as well as an *in vitro* model, to assess their inflammatory potential. These large but respirable GP were inflammogenic in both the lung and the pleural space. MIP-1α, MCP-1, MIP-2, IL-8, and IL-1β expression in the BAL, the pleural lavage, and cell culture supernatant from THP-1 macrophages were increased with GP exposure compared to controls but not with nanoparticulate carbon black (CB). *In vitro*, macrophages exposed to GP showed expression of IL-1β. This study highlights the importance of nanoplatelet form as a driver for *in vivo* and *in vitro* inflammogenicity by virtue of their respirable aerodynamic diameter, despite a considerable 2-dimensional size which leads to frustrated phagocytosis when they deposit in the distal lungs and macrophages attempt to phagocytose them. Our data suggest that nanoplatelets pose a novel nanohazard and structure-toxicity relationship in nanoparticle toxicology.

KEYWORDS: graphene nanoplatelets · aerodynamic diameter · lung · pleura · inflammation · phagocytosis · cytokine activation · inflammasome · ROS

by transit through the ever-narrowing airways of the lung, which they can fully ingest. Fibres are a case where an "accident of aerodynamics" means that very long fibers, if they are thin, can penetrate to the distal lung where macrophages fail to fully engulf the long fibers leading to frustrated phagocytosis and inflammation.[4] Because of their
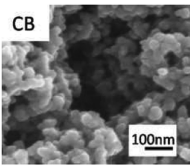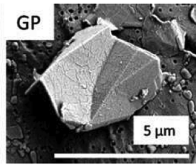
nanoscale dimensions and thinness, nanoplatelets have a much lower Dae than would be expected from their maximum diameter.[2] Attempted uptake of platelet-shaped particles by macrophages in the alveolar region could result in frustrated phagocytosis, inflammation, failed clearance (leading to retention and accumulation of an od dose) and translocation of nanoplatelets to the pleural space.

The lung and the pleural space are key target tissues for diseases related to fiber-shaped particles, for example, asbestos. Exposure to asbestos fibers in poorly regulated workplaces caused a worldwide epidemic of a range of lung and pleural pathologies which include lung fibrosis, lung cancer, pleural plaques, pleural effusion, and pleural mesothelioma.[5] The pleural mesothelium has proven to be uniquely sensitive to fibers. The exact mechanism by which long, biopersistent fiber-shaped particles cause their harmful effects is partially understood and involves a sequence of events including retention of long fibers in the lung due to failed clearance by alveolar macrophages, frustrated phagocytosis, and recruitment of inflammatory cells to the site of fiber retention. Following translocation to the pleura there is retention of longer fibers at stomata at the parietal pleura, inducing inflammation and prolonged interaction between fibers and mesothelial cells. These events culminate in the development of lung and pleural diseases after exposure to long biopersistent fibers.[6,7]

We used a model of pharyngeal aspiration and direct intrapleural injection[7] of the GP to assess the acute and sustained inflammatory response of the lung and the pleural space, respectively. The approach of direct intrapleural injection is justified on the basis that a fraction of all inhaled particles and fibers that deposit in the peripheral lung translocate into the pleural space.[8−10] We do note however that translocation of GP from the distal lung region to the pleural space has yet to be shown. As a compact nanoparticle control for comparison with GP, we used nanoparticulate carbon black (CB) which is also composed of graphene sheets that are present as disjointed layers.[11] We hypothesized that it was the shape in which the graphene was presented that was driving the activity, and that respirable CB would be readily cleared *via* alveolar macrophages from the airspaces and *via* stomata from the pleural space to the mediastinal lymph nodes. In contrast, GP, exceeding the size for complete phagocytosis, would be retained in the lung and, after translocation to the pleural space, would be too large to negotiate the stomata in the parietal pleura and so would initiate inflammation. *In vitro* models were used to elucidate the mechanism leading to inflammation after interactions between GP and macrophages. We assessed the inflammatory potential of GP *via* indicators such as frustrated phagocytosis, cytokine

TABLE 1. Characteristics and Specifications of CB and GP[a]

	CB	GP
Morphology		
Projected diameter [μm] (mean ± s.e.m)	0.01 ± 0.01	5.64 ± 4.56
Layer number	0	1-10
Surface area [m²/g]	253.9	~100
Density [g/cm³]	~1.9	~2
EPR [Arbitrary Units]	451.3±52.2	867.3±77.5
Source	Evonik Degussa GmbH	Cheaptubes.com

[a] Morphology of materials by scanning electron microscopy (SEM). SEM of GP confirms morphology of the platelet shape. EPR measurement to determine generation of oxygen-centred free radicals. Surface area of CB from Donaldson et al.[12]

release, and the involvement of the NALP3 inflammasome.

RESULTS

Characterization of Graphene Nanoplatelets. Characteristics and specifications of CB and GP are summarized in Table 1. Nanoparticulate carbon black (CB) and layered (1−10 layer) graphene nanoplatelet (GP) morphology were examined using scanning electron microscopy (SEM) (Table 1). Electron paramagnetic resonance (EPR) measurements were performed to determine the generation of oxygen-centered free radicals of CB and GP. Results were compared to one another and to a positive Pyrogallol (benzene-1,2,3-triol) control, a spontaneous superoxide anion generator with Tempone H used as a spin trap. Both CB and GP caused a significant increase in free radical generation with GP production increased by 2-fold compared to CB (Table 1). The concentration of soluble metals was measured for CB and GP and showed that both samples possess negligible amounts of soluble contaminating metals that would not be biologically active (Supporting Information Table 1).

Aerodynamics of Nanoplatelets—Calculation of the Aerodynamic Diameter. The gravitational settling speed of a particle is determined by the opposing effects of the gravitational force and the aerodynamic resistance. The aerodynamic drag force depends on the shape and orientation of the particle with respect to its direction of motion. A plate-like particle with uniform

thickness settles under gravity with orientation perpendicular to its direction of motion. If it is not a uniform thickness, it might behave like a spear with a weighted tip (if one edge is relatively heavy) or it might be stable in the perpendicular orientation if the extra weight is central. By taking the gravitational force, the aerodynamic resistance and the circular plate-like shape of a particle into account we derived an expression for the aerodynamic diameter of a plate-like particle as

$$d_{ae} = \sqrt{\frac{9\pi}{16}\frac{\rho}{\rho_0}d_{proj}t}$$

d_{ae} = aerodynamic diameter t = platelet thickness d_{proj} = projected diameter ρ_0 = unit density ρ = density

Using this equation, we can estimate the aerodynamic diameter for plate-like-particles of given dimensions. The size of GP was measured using SEM and light microscopy images and plotted as percentage of GP per projected area diameter in the sample (Tables 1 and 2). The GP consist of several sheets of graphene with a thickness of approximately 10 nm each, therefore their thickness increases to around 0.1 μm, depending on their dispersion. This information was used to calculate the Dae of GP used in this study and shows that they are within the size range of the respirable fraction (Table 2). Full derivation of the Dae equation can be found in the Supporting Information.
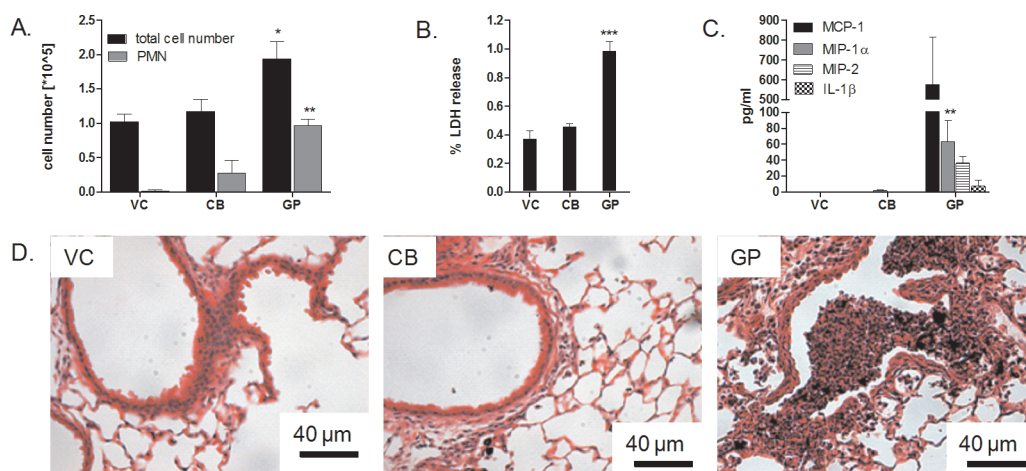
In Vivo. *Acute Pulmonary Inflammatory Response to GP.* To assess the hazard of GP to the lungs, GP were deposited in the lungs by pharyngeal aspiration at a dose of 50 μg per mouse. At 24 h postexposure the total number of bronchoalveolar lavage (BAL) cells was increased significantly in GP-exposed mice compared to vehicle control and mice aspirated with CB (Figure 1A). This increase in cell number was mainly due to an increase in polymorphonuclear leucocytes (PMN), mainly neutrophils and eosinophils in the lavage fluid (Figure 1A). The membrane leakage from cells in BAL was also significantly increased in GP-treated mice (Figure 1B). Concentration of the pro-inflammatory cytokines MCP-1, MIP-1α, MIP-1, and IL-1β were measured in the BAL fluid. All cytokines were elevated after GP treatment compared to VC and CB, however only MIP-2 reached a significant difference (Figure 1C). Histological sections of lungs from mice treated with GP showed granulomatous lesions in the bronchiole lumen and near the alveolar region. VC and CB had a normal histology (Figure 1D) (see Supporting Information for gross pathology of the entire lung section Figure I). The response to CB/GP exposure was investigated one week following exposure and continued to show an increased inflammatory response to GP compared to CB and VC treated animals which was, however, significantly less compared with response at 24 h postaspiration (Supporting Information, Figure II).

TABLE 2. Size Distribution of GP in the Sample Expressed as Percentage of GP per Projected Area Diameter, Aerodynamic Diameter Dae of GP at Various Projected Diameters and a Thickness (t) of 0.1 μm

| % of GP	projected area diameter (d_{proj}) [μm]	aerodynamic diameter [μm] (t = 0.1 μm)
57.4	5	1.33
32.9	10	1.88
6	15	2.30
2.8	20	2.66
0.6	25	2.97
0.3	30	3.26

Acute Pleural Response to GP. The acute pleural inflammatory response was measured 24 h after intrapleural injection of CB and GP. The pleural space was lavaged and a total and differential cell count was performed. Mice exposed to GP showed a significant increase in total cell number compared to vehicle control (Figure 2A) with significant increases in the number of PMN which mainly comprised eosinophils and neutrophils (Figure 2A). Chemokine and cytokine protein levels in the pleural lavage fluid were measured (MCP-1, MIP-1α, MIP-1, and IL-1β) showing that MIP-1α was significantly increased (Figure 2B). Cytospin preparation of lavaged cells showed complete uptake of CB into pleural macrophages (Figure 2C); however, GP, due to their shape and size, could not be fully phagocytosed leading to frustrated phagocytosis. Rosette-like formations of macrophages around GP are a characteristic indicator of frustrated phagocytosis where more than one macrophage surround a large nanoplatelet and share the attempt to phagocytose it (Figure 2C). Histological examination of the parietal pleura showed areas of histiocytic aggregates in mice treated with GP (Figure 2D). The lesion area along the mesothelium was measured and was significantly increased compared to VC and CB at the 24 h time point (VC/CB = 0 μm^2/μm; GP = 19.5 $\pm$ 11.6 μm^2/μm) (n = 3). GP were associated with inflammatory cells along the parietal pleura. The acute inflammatory response has largely resolved 1 week after exposure as can be seen by the decrease in total cell number to a quarter of the number found at 24 h (Supporting Information, Figure III).

Clearance of CB and GP from the Pleural Space to Cranial Mediastinal Lymph Nodes. CB particles were cleared from the pleural space after direct pleural injection *via* stomata to the cranial mediastinal lymph nodes as can be seen in histological lymph node sections after 24 h and 1 week (Figure 3A,B). Twenty-four hours after GP exposure, a few particles could be found in the lymph nodes which indicates prolonged retention in the pleural space (Figure 3A). After 1 week GP have been cleared from the pleural space; however, the amount of clearance appears to be much less compared to that of CB (Figure 3B). Quantification of

Figure 1. Pulmonary inflammatory response to CB and GP 24 h postaspiration. (A) Total cell number and total granulocyte number in the lavage fluid following exposure to CB and GP. **(B)** Measurement of the membrane leakage as LDH levels in the lavage fluid. **(C)** Concentration of the chemokines MCP-1 and MIP-1α as well as cytokines MIP-1 and IL-1β in BAL. (*) $P < 0.05$, (**) $P < 0.01$, (***) $P < 0.001$ compared to vehicle control. **(D)** Lung histology 24 h postaspiration. Ganulomatous lesion was present in the bronchiolar lumen after GP exposure but normal lung pathology was seen in the CB treated mice which is comparable to VC.
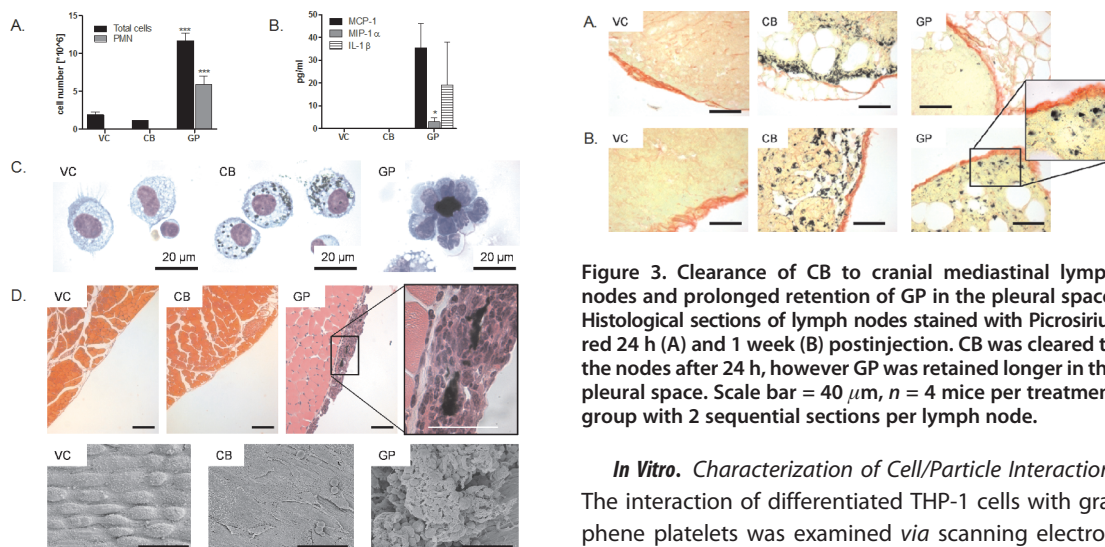
Figure 2. Pleural inflammatory response to CB and GP 24 h post-treatment. (A) Total cell number and total granulocyte number after pleural injection of 5 μg of CB and GP. **(B)** Concentration of the chemokines MCP-1 and MIP-1α as well as cytokines IL-1β in pleural lavage. (*) $P < 0.05$, (***) $P < 0.001$ compared to vehicle control. **(C)** Representative images of pleural macrophages from untreated mice and mice treated with CB and GP. Intrapleural injection of GP led to the formation of rosette-like cell/particle aggregations indicating frustrated phagocytosis. **(D)** Sections of chest wall were stained with both haematoxylin and eosin (H&E) at 24 h postinjection to identify an inflammatory response on the mesothelial cell layer of the parietal pleura ($n = 3$). Pleural thickening can be seen after GP treatment, with an insert highlighting GP associated with inflammatory cells. Scale bar = 100 μm, insert = 20 μm. SEM micrographs show aggregations of inflammatory cells after GP treatment but normal mesothelial cell layer after VC and CB treatment (Figure 2 bottom panels). Scale bar = 20 μm.

the GP size cleared to the lymph nodes could not be performed because of the difficulty of identifying individual platelets of GP in the section.
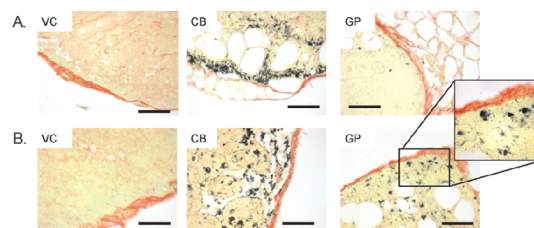
Figure 3. Clearance of CB to cranial mediastinal lymph nodes and prolonged retention of GP in the pleural space. Histological sections of lymph nodes stained with Picrosirius red 24 h **(A)** and 1 week **(B)** postinjection. CB was cleared to the nodes after 24 h, however GP was retained longer in the pleural space. Scale bar = 40 μm, $n = 4$ mice per treatment group with 2 sequential sections per lymph node.

In Vitro. *Characterization of Cell/Particle Interaction.* The interaction of differentiated THP-1 cells with graphene platelets was examined *via* scanning electron microscopy (SEM) and transmission electron microscopy (TEM). The SEM images revealed that GP exceeding a size of approximately 15 μm projected diameter could not be fully phagocytosed by THP-1 cells and therefore led to frustrated phagocytosis (Figure 4A,B). Complete uptake of smaller GP could be imaged using TEM as shown in Figure 4B.

GP-Mediated Loss of Membrane Integrity of THP-1 Macrophages and Depletion of Reduced Glutathione. Release of LDH was used as an indicator of cell viability and measured after 24 h exposure of THP-1 macrophages to CB and GP. A concentration range of 1 μg/cm^2, 5 μg/cm^2, and 10 μg/cm^2 of GP was used, and concentrations of 5 μg/cm^2 and higher significantly increased LDH release while CB exposure at the same concentrations did not (Figure 5A). An explanation for loss of membrane integrity could be the generation of reactive oxygen species and so the levels of free thiol groups, predominantly GSH, were measured as an
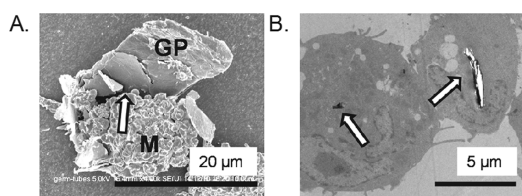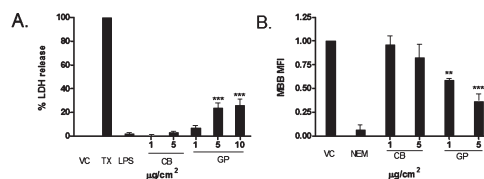
Figure 4. Cell/particle interactions to examine the uptake of GP on the surface using SEM and inside of the cells using TEM following 4 h exposure to GP. (A) SEM and (B) TEM of GP-exposed THP-1 cells. (A) SEM showing the attempted uptake of a GP by THP-1 macrophages (M). The arrow indicates the lip of the unclosed phagosome showing incomplete internalization of the GP producing frustrated phagocytosis. (B) TEM shows that small GP ($\leq 5 \mu m$) could be entirely internalized (arrows).

Figure 5. Determination of LDH release and the decrease in free thiol groups as indications of cell toxicity and oxidative stress. (A) Significant release of LDH after 24 h exposure to GP while CB had no significant effect on LDH. Data were expressed as mean ± s.e.m, $n = 5$. (B) Mean fluorescence intensity (MFI) of monobromobimane (MBB) as indicator for levels of free thiol groups. GP exposure significantly reduced the MFI of MBB at all concentrations measured. Data were expressed as mean ± s.e.m, $n = 4$. (**) $P < 0.01$, (***) $P < 0.001$ compared to vehicle control.

Figure 6. Data providing evidence consistent with activation of the Nalp3 inflammasome, and pro-inflammatory cytokine expression on GP, CB, and LPS treatment. (A) IL-1β concentration in the supernatant of THP-1 cells exposed to LPS, CB, and GP. LPS (1 μg/mL) as well as GP at all concentrations led to a significant increase in IL-1β expression, whereas CB treatment had no effect. Phagocytotic uptake of GP was inhibited by cytochalsin D which led to a significant reduction of IL-1β expression in GP exposed cells. This effect was not observed in LPS treated cells. IL-1β expression after LPS and GP exposure was significantly reduced by inhibition of K+ efflux and diphenylene iodonium (DPI), an NADPH oxidase inhibitor. Data were expressed as mean ± s.e.m, $n = 4$. (B) Four cytokines (MCP-1, IL-8, IL-1β and MIP-1α) out of 11 tested were significantly upregulated after a 24 h GP exposure. CB treatment did not lead to a significant increase in any of the cytokines measured. Data were expressed as mean ± s.e.m, $n = 3$. (*) $P < 0.05$, (**) $P < 0.01$, (***) $P < 0.001$ compared to vehicle control. (#) $p < 0.05$, (##) $p < 0.01$, (###) $p < 0.001$ compared to vehicle control.

indicator for oxidative stress, using the fluorescence probe, monobromobimane. After 4 h of GP exposure the levels of free thiol groups were significantly lowered compared to the vehicle control (Figure 5B). CB did cause a significant change in the levels of free thiol groups.
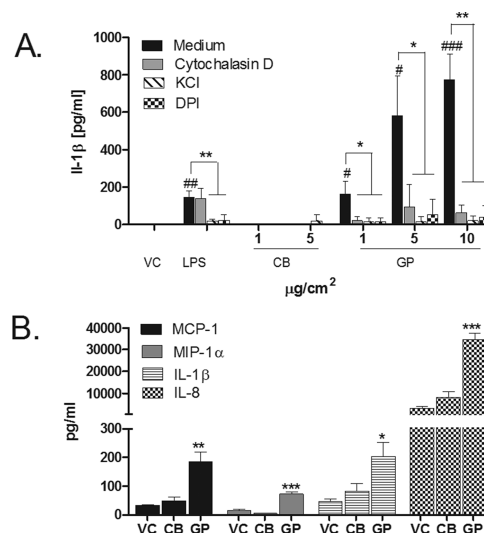
Activation of the NALP3 Inflammasome and Pro-inflammatory Cytokines after GP Exposure in Vitro. We measured the concentration of IL-1β in the supernatant of THP-1 cells exposed for 24 h to either LPS, CB (1 and 5 μg/cm^2), or GP (1, 5, and 10 μg/cm^2). LPS as well as all concentrations of GP lead to a significant increase in IL-1β expression, whereas CB treatment had no effect (Figure 6A). To investigate if the attempt to phagocytose GP was involved in upregulating IL-1β expression, phagocytosis was inhibited *via* disruption of actin filaments using cytochalasin D. The inhibition of phagocytosis significantly reduced IL-1 β expression at all concentrations of GP; however, cytochalasin D had no effect on the level of IL-1 β released by THP-1 cells exposed to LPS since its action is not dependent on phagocytic processes (Figure 6A). Additional mechanisms involved in the activation of the NALP3 inflammasome are decreased intracellular K+ linked to an efflux of K+ and generation of ROS. By blocking the efflux of K+ *via* increasing extracellular K+ concentration and the inhibition of generation of ROS *via* inhibition of NADPH oxidase using DPI, the expression of IL-1β was significantly reduced in both LPS and GP exposed cells (Figure 6A). To further assess which cytokines were involved in acute inflammation after particle exposure, a cytokine bead array was performed. The selected panel of cytokines was TNF, IL-6, IL-8, IL-1β, MCP-1, RANTES, MIP-1α, basic FGF, IL-13 and TGF-β. MCP-1, IL-1, MIP-1α, and IL-1β were all significantly increased after GP exposure with no effect of CB exposure on these cytokines (Figure 6B).

DISCUSSION

Although Duch *et al.*[12] have studied the biocompatibility of GP in the mouse lung from the point of view of biomedical/therapeutic application of GP, we believe that ours is the first peer-reviewed publication to address the public/occupational health hazard of GP in

rat lung from the point of view of aerodynamic deposition and the cellular responses in lung. We further elucidate the mechanism leading to GP-induced inflammation, using *in vitro* methods and a macrophage cell line. Nanoparticulate carbon black (CB) was used as a compact graphene nanoparticulate control and was aspirated at a mass dose found to be noninflammatory in previous studies.[13]

The atypical platelet-like shape of the GP particles attracted our attention as they may pose a new risk to the respiratory system after inhalation. Nanoplatelets exhibit specific material properties that could be important for biological interactions. Among these are surface area, surface chemistry, and lateral dimensions. Owing to their platelet shape, they have an exceptionally high surface area per unit mass which is much greater than that of graphite and of carbon nanotubes.[14] The lateral dimensions of a material play an important role in biological interaction and determine the nature and consequences of cellular uptake and subsequent clearance.

Thus far, in the field of particle toxicology, the fiber pathogenicity paradigm has been stated as the most robust structure–activity relationship, and it has frustrated phagocytosis of long fibers as the center of the pathobiological mechanism.[15] This structure–activity relationship focuses on fibers that are long, thin, and biopersistent, having an aerodynamic diameter that makes them respirable.[16] This structure–activity relationship however does not take sheet/platelet shape particles into account and therefore has to be reconsidered in the light of these new materials.

To be most harmful to the respiratory system, particles require an aerodynamic diameter small enough to penetrate beyond the ciliated airways, that is, they need to be respirable. Deposition occurs under the effects of gravitational force, aerodynamic resistance, interception, and impaction which together determine the site of deposition in the lungs.[17] The aerodynamic diameter is the index that is calculated from these parameters and determines the respirability of a particle and the site of deposition.[3] Plate-shaped particles are not common in industry, and so exposure is limited, but does occur in the talc and nanoclay industries where there are plate-like particles.[18,19] However the nanotechnologies have the potential to produce a range of different nanoplatelet-shaped particles. In this study we calculated the aerodynamics of commercially available nanoplatelets by taking into consideration the gravitational settling force and aerodynamic resistance perpendicular and parallel to motion, and utilized an equation derived from the tenets of aerosol physics to estimate the aerodynamic diameter of platelet-like particles of the dimensions evident in our GP sample. This demonstrated that a platelet-shaped particle with a projected area diameter of 25 μm and a thickness of 0.1 μm has an aerodynamic diameter of about 3 μm, which is within the respirable size fraction of particles that deposit beyond the ciliated airways. These calculations are in line with the aerodynamic sizes reported recently in Sanchez et al.[2] which also showed images suggesting that GP might lead to frustrated phagocytosis in macrophages.

On the basis of our determination that the GP samples used within these experiments were all respirable, we assessed the inflammatory potential of GP. Mice were exposed via pharyngeal aspiration and pleural injection to CB and GP for 24 h and 1 week. CB and GP are composed of the same material, graphene, and were both respirable but differed in their shape, which resulted in very different effects in the lung and the pleural space. CB did not cause any inflammatory response and was comparable to vehicle control in all assays, whereas GP caused extensive recruitment of inflammatory cells, including macrophages and granulocytes into the lung and pleural space after 24 h exposure. Inflammation waned 1 week post-exposure but continued to be significantly greater in total cells and granulocyte number than the vehicle control. The response to GP in the lung and the pleural space was similar to the response seen after aspiration exposure and intrapleural injection of long MWCNT using the same method.[7,20] Recent studies revealed that long CNT, due to their fiber-like structure similar to asbestos show an asbestos like pathogenicity and raised concern that exposure to CNT may lead to mesothelioma.[21] Our results show that long fibers are not the only extended particles with low Dae that are able to induce inflammation in the lung and the pleural space, but that platelet like particles with a low Dae have similar potency. The induction of acute and chronic inflammation is regulated by the release of cytokines and chemokines that invoke leukocyte recruitment. Analysis of BAL and pleural lavage fluid revealed elevated levels of MCP-1, MIP-1α, IL-8, and IL-1β after GP but not CB. MCP-1 and MIP-1α have been reported to contribute to the initiation and outcome of inflammation in the lung and in pulmonary alveolar macrophages after exposure to stone-wool and crocidolite asbestos.[22] MCP-1 has further been identified to play a major role in lung leukocyte infiltration[23] and serves as a marker for the diagnosis of malignant pleural mesothelioma.[24]

The main mechanisms by which long, fiberlike particles cause harmful health effects in the pleura are the failed clearance of longer fibers through stomata in the parietal pleura and subsequent retention in the pleural space, frustrated phagocytosis of pleural macrophages, and the involvement of the NALP3 inflammasome.[25] We therefore investigated the retention of GP in the pleural space by examining the most caudal, posterior intercostal region of the parietal pleura, documented to have the highest abundance of stomata.[7,26] Interstitial incorporation of asbestos fibers and coal dust occurs in these areas and so they are described as potential starting points for the development of mesothelioma.[11] In support of this hypothesis we observed extensive accumulation of inflammatory cells in these areas on the parietal pleura where GP were retained. To determine the clearance pathway of CB and GP, we examined the particle burden in cranial mediastinal lymph nodes (LN). Pleural fluid is drained

through the parietal stomata *via* the lymphatic system to LN.[7,27] CB was readily cleared to the mediastinal lymph nodes after 24 h as could be seen in histological sections. In comparison, few GP had reached the LN after 24 h, confirming retention of GP in the pleural space. After 1 week however, a higher number of GP could be identified in the mediastinal LN sections, which may explain the reduced inflammation seen 1 week after intrapleural exposure. Brakeage of GP into smaller fragments after 1 week could explain the time-dependent clearance of GP to the LNs. We noted that the accumulation of GP in the LN seen at 1 week, while evident, was less than that seen 1 week after CB, suggesting that there is a substantial fraction of the GP dose that remains retained in the pleural space beyond one week.

The role of frustrated phagocytosis, a mechanism by which long fibers produce inflammation, has been examined in a number of studies[28,29] and has been accepted as a contributing mechanism to the toxic effects of long fibers. Due to the extended shape of GP, we hypothesized that the uptake of GP by macrophages could be impaired leading to frustrated phagocytosis. Examination of pleural macrophages in the lavage fluid showed clear signs of frustrated phagocytosis after GP exposure, whereas CB was fully taken up. This took the form of GP incompletely enclosed by macrophages and "rosettes" of up to five or six macrophages surrounding a single large platelet where all of the macrophages are in a state of frustrated phagocytosis.

To further investigate the interaction of macrophages with GP, we treated cells of a differentiated monocytic cell line, THP-1, with GP and examined phagocytosis using scanning electron microscopy (SEM) and transmission electron microscopy (TEM). Frustrated phagocytosis could be observed in SEM images, showing GP only partly phagocytosed by macrophages. TEM revealed that only small GP ($\leq 5\ \mu$m) were fully taken up. The membrane integrity of THP-1 cells after 24 h GP exposure was also significantly impaired in a dose-dependent manner. We also determined the generation of oxygen-centered free radicals by GP and CB using EPR. CB as well as GP generated a significant amount of free radicals, and GP generated approximately double that produced by CB. Therefore free radicals are possibly involved in the pro-inflammatory effects seen *in vivo* and *in vitro* with GP compared to CB, although it is not likely that intrinsic free radical activity explains the extra potency of GP. We went on to determine the oxidative status of THP-1 cells by measuring the decrease in free thiol groups, mainly reduced glutathione after CB and GP treatment. Glutathione/glutathione disulfide is the major redox couple in cells, and its tight regulation is critical in antioxidant defense and regulation of cellular events.[30] Glutathione is the most abundant

low-molecular-weight thiol, and the loss of free thiol can be measured *via* loss of monobromobimane fluorescence.[30] Exposure of THP-1 cells to GP lead to a significant decrease in free thiol groups in a dose-dependent manner. Depletion of the antioxidant defense system by pollutants[31] and respirable fibers[32] has been shown to result in oxidative stress and the activation of transcription factors including NF-κB.[33] NF-κB regulates the transcription of inflammatory genes, including IL-1β, MIP-1α, and MCP-1.[34] We measured a panel of acute-phase cytokines involved in the inflammatory response after exposure of THP-1 cells to CB and GP; 4 out of 11 different cytokines measured, MCP-1, IL-8, IL-1β and MIP-1α, were significantly elevated after GP exposure. The pro-inflammatory cytokine and neutrophil chemotaxin IL-8 has been shown to be elevated in airway epithelial cells and serum[35] as well as alveolar macrophages[36] of asbestos-exposed individuals.[35] IL-1β is known to be upregulated after asbestos, silica, and CNT exposure[37,38] and has been implicated in frustrated phagocytosis and the NALP3 inflammasome activation.[39] The underlying mechanism by which frustrated phagocytosis of long fibers induces acute and chronic inflammation is poorly understood. Recent studies however identified the NALP3 inflammasome complex as an important component of the molecular pathway by which cells sense foreign bodies like asbestos fibers and initiate an inflammatory response. The inflammasome is a multiprotein complex consisting of nucleotide-binding oligomerization domain (NOD)-like receptors (NLR) which is activated *via* damage-associated molecular patterns (DAMPs) and forms a complex with apoptosis-associated speck-like protein containing a caspase-recruiting domain (CARD) and pro-caspase 1. Activation of caspase 1 leads to expression of IL-1β and IL-18, which mediate pro-inflammatory effects.[40] The inflammasome can be activated *via* different pathways including low intracellular potassium concentration[41], reactive oxygen species produced by NALP3 activators *via* NADPH oxidase,[42] frustrated phagocytosis[39] and phagosomal destabilization.[38] Since GP exposure led to an increased production of IL-1β, we explored the possibility that GP promote inflammation by activating the inflammasome pathway. To delineate the GP-induced signaling pathway leading to inflammasome activation, IL-1β production after GP exposure was compared to CB and LPS induced IL-1β release in cell culture medium and medium supplemented with inhibitors for phagocytosis, ROS generation, and potassium efflux. We investigated whether phagocytosis is needed to trigger inflammasome activation by disrupting actin filaments *via* cytochalasin D.[37] Inhibition of phagocytosis significantly reduced IL-1β expression after GP treatment, but had no effect on LPS induced IL-1β production, which is not mediated *via* phagocytosis. We further provided evidence that GP activity is

blocked by inhibiting efflux of K+, which is necessary for NALP3 inflammasome activation. Reduction of IL-1β production was also achieved by inhibition of the NADPH oxidase supporting the hypothesis that ROS are generated *via* phagocytosis of GP through the activation of the reduced form of NADP. We therefore carried out limited studies which, while providing data consistent with activation of the NALP3 inflammasome by GP, require more detailed and extensive studies to confirm this impression.

Collectively, our data show that large nanoplatelets can have a small enough Dae to be respirable and to deposit beyond the ciliated airways where macrophages are the only mode of clearance, but are too large to be completely phagocytosed by macrophages. They, therefore are likely to cause an inflammatory response in the airspaces and be retained, similar to the response seen after long asbestos and other long fiber-like structures[7] (Schinwald *et al.*, manuscript under submission). If, like long fibers they are capable of reaching the pleural space, they will be retained there as they will be too big to negotiate the stomata and, with sufficient dose, they will cause pleural inflammation and pleural pathology over time if they are sufficiently biopersistent.

Our study also provides information regarding the mechanism by which the inflammatory response to GP was initiated using *in vitro* models. Four cytokines have been detected to be involved in the onset of inflammation after GP exposure (MIP-1α, MCP-1, IL-8, and IL-1β). While IL-1β may have been activated *via* the NALP3 inflammasome complex, more research is needed to confirm this. We further emphasized the importance of phagocytosis and subsequent ROS generation in the activation of IL-1β release.

We mainly focused on the acute inflammatory reaction in the lung and the pleural space up to 7 days and the data showed a decrease in the severity of inflammation after 7 day treatment which suggests degradation of GP into smaller fragments which could then be cleared *via* alveolar/pleural macrophages. A study of the chronic effects of GP exposure, preferably after inhalation exposure is warranted to investigate biopersistence and effects after inhalation compared to the instillation models used here. In this study we focus on the morphology of the GP, rather than the graphene oxidation state, in regards to pro-inflammatory effects especially frustrated phagocytosis. The argument of frustrated phagocytosis of GP is based on shape rather than chemistry, as is the argument of long fibers-elicited frustrated phagocytosis, which is an issue of fiber length, not composition[6,43] Future studies on different GP samples from different sources should examine the effect of the surface chemistry/oxidation state, which might have an additional effect; however, we consider that any such effect will be in addition to the shape effect.

CONCLUSION

This study highlights the importance of particle shape as a driver for *in vivo* and *in vitro* toxicity and introduces a new shape that may pose an unusual risk to the lungs and the pleural space after inhalation exposure. We suggest that sheet/platelet-shaped particles with nanoscale thickness can be very large in two dimensions but possess a low Dae. Thus they have the potential to cause adverse health effects and therefore warrant further investigation. We further suggest that lateral dimensions are the driving properties in pathological response to GP and that these also require more research. It also seems likely that layer thickness and the subsequent role that this plays in rigidity is a key factor but was not investigated here. On the basis of the above understanding of the probable mechanisms, we suggest that potential risks to humans from graphene platelet exposure could be minimized by manufacturing graphene platelets small enough to be phagocytosed by macrophages. Our initial data also suggest that the GP are not fully biopersistent, and clear slowly to the mediastinal lymph nodes. Further work is needed to determine the extent of GP biopersistence and its impact on pathogenicity.

MATERIAL AND METHODS

Characterization of Nanoparticle Carbon Black (CB) and Graphene Nanoplatelets (GP). Carbon Black (Printex 90) was provided by Evonik Degussa GmbH in Germany. It was used as an amorphous carbon particle control. Graphene nanoplatelets grade 2 (GP) produced by chemical exfoliation were purchased from cheaptubes.com. GP have a surface area of about 100 m²/g, a density of ~2.0 g/cm³, an average thickness of approximately 10 nm and an average diameter of 5 μm based on manufacturers description. One of the GP consists of several sheets of graphene, and GP are therefore classified as few-layer graphene. Physical characteristics were determined using light microscopy and scanning electron microscopy (SEM). The levels of endotoxin in the sample suspension were evaluated by the Limuluss Amoebocyte Lysate assay (Lonza) according to manufacturer's description using supernatant of CB and GP suspension to avoid interference of particles with the assay. No endotoxin level were detected in the samples. CB and GP stock solution was prepared at 1 mg/mL in 0.5% BSA/saline for *in vivo* work or cell culture medium without FBS for *in vitro* work and dispersed by sonication in an ultrasonicating water bath at 230 V, 50 Hz, 350W (FB11002, Fisherbrand, Thermo Fisher Scientific, Inc., MA, USA) for 6 h to break up aggregates.

Scanning Electron Microscopy of CB and GP. CB and GP were dispersed in 0.1% BSA (heat-shocked fractionate) (Sigma-Aldrich, Poole, UK)/saline at a concentration 50 μg/mL by ultrsonication. The suspension was filtered onto an Isopore membrane filter (Millipore), dried, and gold sputter coated. Scanning electron microscopy was carried out using a Hitachi S-2600N digital scanning electron microscope (Oxford Instruments, Oxfordshire, UK).

Light Microscopy of CB and GP. For light microscopy images a concentration of 50 μg/mL was used to demonstrate the dispersion of the materials. A 10 μL aliquot of CB or GP solution were mixed with 10 μL of glycerol (Sigma-Aldrich, Poole, UK) to reduce the motion of the GP. The suspension was placed on glass slide and covered with a glass coverslip and sealed.[7] Images were captured at 100× magnification using QCapture Pro software (Media Cybernetics). A total of 300 GP/GP-aggregates were measured according to their projected area diameter by using a graticule. The size was plotted per length category.

Electron Paramagnetic Resonance. CB and GP were diluted to a final concentration of 50 μg/mL in Hanks Balanced Salt Solution (HBSS) (Sigma-Aldrich, Poole, UK) and sonicated for 1 h. HBSS and 1 mM Pyrogallol (Sigma), a known superoxide generator were diluted in Hanks buffer and used as negative and positive controls, respectively. Peroxynitrite, superoxide, and peroxyl radical release were detected using spin trap Tempone-H (Alexis Biochemicals, San Diego, CA). Tempone-H was added to the samples and controls to give a final concentration of 1 mM. EPR spectra were measured after 60 min incubation at 37 °C using the following instrumental conditions: Microwave frequency, 9.39 GHz, magnetic field, 3355 G; sweep width, 55 G; sweep time, 30 s; number of passes, 1; modulation amplitude, 1500 mG; receiver gain, 1E1; phase, 180; microwave frequency, 9.30−9.55 GHz. Intensity values of the highest spectra peak were recorded and graphed against each other (arbitrary units).

ICP−MS Analysis. For quantification of contaminating metals, the supernatant of 1 mg/mL of each sample were analyzed using the technique of inductively coupled mass spectrometry (ICP−MS). The CB and GP suspension was made up in 0.5% BSA/saline to be consistent with experimental conditions. Supernatant was collected from a 1 mg/mL solution of each sample, after overnight mixing, by centrifugation at 13 000 rpm for 30 min. Samples were analyzed by ICP−MS using an Agilent 7500ce (with octopole reaction system), employing an rf forward power of 1540 W and reflected power of 1 W, with argon gas flows of 0.82 L min^{-1} and 0.2 L min^{-1} for carrier and makeup flows, respectively. Sample solutions were taken up into the micromist nebulizer by peristaltic pump at a rate of 0.06 rps (approximately 1.2 mL min^{-1}). The gas flow for the helium mode was 6.5 mL min^{-1}. Skimmer and sample cones were made of nickel. The instrument was operated in spectrum multitune acquisition mode, and five replicate runs per sample were employed. Each mass was analyzed in fully quant mode (three points per unit mass). ^{107}Ag, ^{27}Al, ^{111}Cd, ^{59}Co, ^{52}Cr, ^{63}Cu, ^{56}Fe, ^{55}Mn, ^{60}Ni, ^{208}Pb, and ^{64}Zn were analyzed in "nogas" mode then ^{56}Fe, ^{60}Ni, ^{52}Cr, ^{63}Cu, and ^{66}Zn were further analyzed in helium mode to remove any polyatomic interferences.

In Vivo. *Experimental Animals.* Nine week old female C57BL/6 strain mice (Harlan, UK) were used in this study. Mice were kept in a group size of five in standard caging with sawdust bedding within a pathogen-free Home Office approved facility. Mice were maintained on a normal 12 h light and dark cycle. Prior to the treatment mice were kept for 7 days in the facility to acclimatize. The work was carried out by staff holding a valid UK Home Office personal license under a Home Office approved project license.

Pharyngeal Aspiration and Broncho-Alveolar Lavage. The given particle dose for pharyngeal aspiration was 50 μg per mouse of CB and GP in 0.5% BSA/saline. Vehicle control was 0.5% BSA/saline. Mice were anesthetized with isoflurane and the tongue was gently held in full extension while 50 μL of particle suspension was pipet onto the base of the tongue.[44] The tongue was held extended until at least two breaths were complete. To stimulate inhalation and to induce a gasp reflex the nasal cavities of the mice were covered. Mice were observed until full recovery.

Mice were sacrificed 24 h and 1 week postexposure of a single dose by terminal anesthesia by injection of 0.5 mL of pentobarbitone (200 mg/mL) into the peritoneal cavity followed by exsanguinations *via* the abdominal aorta. After the pleural cavity was lavaged (see Intrapleural Injection and Pleural Lavage section) the thoracic cavity was exposed and the trachea cannulated using a 23 gauge needle and ligated. The lungs were lavaged three times with 800 μL of ice-cold sterile saline. The first lavage was retained separately and the subsequent lavages were pooled.

Intrapleural Injection and Pleural Lavage. Samples were prepared by ultrasonication as described and injected into the pleural cavity of female C57Bl/6 mice (aged 8 weeks) using a sleeve over the tip of a 27G to prevent the needle to pass through the pleural space into the lung. The concentration of each treatment was 50 μg/mL which equates to a single dose of 5 μg per mouse and an injected volume of 100 μL per mouse. Mice were euthanized after 24 h ($n = 6$) and 7 days ($n = 4$) by asphyxiation in 100% CO_2. The pleural space was lavaged with three 1 mL washes of sterile saline and kept on ice.

Differential Cell Count/Total Protein and Lactate Dehydrogenase Measurement. To separate the cellular fraction from the supernatant the lavage fluid from BAL and pleural lavage was centrifuged for 5 min at 2000g at 4 °C in a Mistral 3000i centrifuge (Thermo Fisher Scientific, Inc., MA, USA). Total cell count was performed using a NucleoCounter (ChemoMetec, 7 A/S, Allerød, Denmark) and cyto-centrifugation with following Diff-Quik staining using Diff-Quik stainset (Dade Behring Gmbh, Marburg, Germany) were prepared for differential cell counts. In the supernatant, membrane integrity using the Cytotoxicity Detection Lactate Dehydrogenase kit (Roche Diagnostics Ltd., Burgess Hill, UK) and protein content using the bicinchoninic acid (BCA) protein assay (Sigma-Aldrich, Poole, UK) were measured following the manufacturer's instructions.

Dissection of Lung, Diaphragm and Chest Wall. For histological examination the lungs and heart were removed on-block and fixed by installation of 10% ice-cold formalin without foregoing lavage and submerged in fixative for a period of 4 h prior to processing. The heart was removed and the lung separated into individual lobes and transferred to 70% ethanol for 24 h. The tissue was embedded in paraffin, sectioned and stained with H&E to show gross pathology and Pico-Sirius Red (PSR) to show collagen deposition. Serial images were taken at 2.5× magnification using QCaputre Pro software (Media Cybernetics, Inc., MD, USA) and seamlessly realigned using Adobe Phtotoshop CS3, version 10.0.1 (Adobe Systems Inc.) to show the entire section of the lungs. Images at 20× magnification were taken to show higher maginification areas of the lung sections.

The diaphragm and the lower right posterior portion of the chest wall, approximately an area of 1 cm × 0.5 cm along the spine was cut out from the mice after lavage, washed in ice-cold saline, and fixed for 4 h in 30% formalin. The tissue was excised from the surrounding tissue and either embedded in paraffin, sectioned, and stained with haematoxylin and eosin (H&E) for gross pathology or prepared for scanning electron microscopy (SEM).

Methodology for Lesion Quantification. Images from chest wall section were taken at 10× magnification using QCapture Pro software (media Cybernetics Inc., MD, USA). Photoshop CS3 (Adobe systems Inc., CA, USA) was used to seamlessly realign the images to give a high resolution image of the large sections of chest wall. To quantify the lesion area per unit chest wall length (mm^2/mm), the length of the each section along the mesothelium and the lesion area was measured using calibrated Image-Pro Plus software (Media Cybernetics Inc., MD, USA).

Scanning Electron Microscopy. Scanning electron microscopy was carried out using a Hitachi S-2600N digital scanning electron microscope (Oxford Instruments, Oxfordshire, UK). Tissue was prepared using tetroxide staining, critical-point dried, and gold sputter coated.

Chemokine and Cytokine Measurement. Chemokines MCP-1 and MIP-1α and cytokines MIP-2 and IL-1β were measured in nondiluted BAL and pleural lavage fluid following the manufacturers' instructions (Quantikine kit of R&D systems).

In Vitro. *Cell Culture.* The immortalized human monocytic cell line THP-1 was used for *in vitro* studies. THP-1 cells were cultured in RPMI media supplemented with 10% heat inactivated FBS, 1% penicillin/streptomycin and 1% L-glutamine (PAA, Austria). Prior to each treatment the cells were differentiated to macrophages using 10 ng/mL phorbol 12-myristate

13-acetate (PMA) (Sigma) for 2 days at 37 °C in 5% CO_2 atm as previously described.[45]

Measurement of Membrane Integrity. The conversion of lactate to pyruvate was detected using the Cytotoxicity Detection Lactate Dehydrogenase kit (Roche Diagnostics Ltd., Burgess Hill, UK) following the manufacturer's instructions. THP-1 cells were seeded in 24-well plates at a density of 1×106/mL in 500 μL medium containing 10% FBS and differentiated as described above. Prior to treatment the cells were washed with PBS and 500 μL of 1% FBS RPMI medium was added to each well. Cells were treated for 24 h with either lipopolysaccharide at a final concentration of 1 μg/mL, NPCB at 1 μg/cm^2 or 5 μg/cm^2 and GP at a concentration range of 1 μg/cm^2, 5 μg/cm^2, and 10 μg/cm^2 in cell media and media supplemented with either cytochalasin D at a concentration of 0.2 μM (Enzo Life Sciences), potassium chloride at 30 mM (Sigma), and diphenyleneiodonium chloride at 15 μM (Sigma). Triton X (0.1%, Sigma) was used as a positive control, and the cells were incubated with Triton X for 30 min. After the treatment the supernatant was centrifuged for 5 min at 2000g, transferred, centrifuged again for 5 min at 13000g and used for activity assay according to manufacturer's instructions. A microplate reader (BioTek SynergyHT) was used to measure the optical density at 490 nm. Results are given as the mean $\pm$ sem of five independent experiments.

Cytokine Bead Array. The supernatant of untreated cells and cells treated with 5 μg/cm^2 CB and GP in medium was used to screen for 11 cytokines important in acute inflammation and apoptosis to identify cytokines unregulated after treatment. The cytokine levels were measured using a BD Cytometric Bead Array Flex Set. The flex set included the human soluble protein buffer master kit and bead numbers D9, A7, A9, B4, D8, D4, B9, C5, E6, B6 representing the cytokines TNF, IL-6, IL-8, IL-1, MCP-1, Rantes, MIP-1α, basic FGF, IL-13 and TGF-β.

Twenty-five microliters of mixed capture antibodies were added to 50 μL of each supernatant or standard in a 96 well plate and incubated for 1 h at room temperature. Detection reagent was added to each well and incubated for 2 h at room temperature. After centrifugation at 1500g for 5 min the supernatant was removed and wash buffer was added to each well and agitated for 5 min for resuspension of the beads. BD FACSArray Bioanalyzer was used to measure the fluorescence intensity and FACP array software was used for analysis. The concentration of each cytokine was calculated using the standard curve and expressed as pg/mL. Results are given as the mean $\pm$ sem of three independent experiments.

ELISA. The supernatant of all treatment groups (including supplemented media) was further used to measure the expression of IL1-β using human IL1-β/IL-1F2 DuoSet (R&D Systems Europe Ltd., Abingdon, UK) according to manufacturer's description. Results are given as the mean $\pm$ sem of five independent experiments.

Detection of Reduced Glutathione (GSH) as Indicator of the Oxidative Status of Cells. The oxidative status of glutathione can be detected *via* monobromobimane (MBB), which becomes fluorescence after binding nonenzymatically free thiol group of GSH. THP-1 cells were seeded in 12-well plates at a density of 0.5×105/mL in 2.5 mL medium containing 10% FBS and differentiated as described above. Prior to treatment the cells were washed with PBS, and 2.5 mL of 1% FBS RPMI medium was added to each well. Cells were treated for 4 h with either NPCB or GP at 1 μg/cm^2 or 5 μg/cm^2 in cell media. N-Ethyl-maleimide (NEM) (100 μM, Sigma-Aldrich) was used as a negative, depletion of reduced glutathione. Supernatant and cells were transferred into falcon tubes and centrifuged for 3 min at 1500g. PBS was added to the pellet and centrifuged for 3 min at 1500g and repeated twice. A 150 μL portion of 50 μM monobromobimane (MBB) (Sigma-Aldrich) was added to the pellets and incubated for 10 min at 37 °C. Controls were included in all measurements and comprised untreated/unstained and untreated/stained samples as well as treated/unstained samples. The dye was detected using a BD LSRFortessa flow cytometer. MBB was excited by a violet laser (405 nm, 50 mW) and the emission was detected through a 455/40 filter. FlowJo software (Tree Star Inc.) was used for analyzing the data. Gating was based on FCS/SCS and the data is expressed as mean fluorescence intensity. The mean value of the blank sample was subtracted from the stained samples. Results are given as the mean $\pm$ sem of four independent experiments.

Scanning/Transmission Electron Microscopy. THP-1 cells were differentiated as described above and seeded in 24 well plates on Thermanox Plastic Coverslips (NUNC, Rochester, NY USA) at a density of 1×106/mL. The cells were treated with 1 μg/cm^2 and 5 μg/cm^2 NPCB and GP for 4 days at 37 °C in 5% CO_2 atm and washed 5$\times$ with 0.1 M sodium cacodylate (pH 7.2) buffer. Overnight fixation was done in 3% glutaraldehyde/0.1 M sodium cacodylate (pH 7.2) buffer. After fixation the cells adherent to the coverslips were washed in sodium cacodylate buffer, postfixed in 1% osmium tetroxide in 0.1 M sodium cacodylate buffer for 45 min, critical-point dried, and gold sputter coated.

Samples for TEM were embedded in Araldite resin. Sections 1 μm thick were cut on a Reichert OMU4 ultramicrotome (Leica Microsystems (UK) Ltd., Milton Keynes), stained with Toluidine Blue and viewed in a light microscope to select suitable areas for investigation. Ultrathin sections, 60 nm thick were cut from selected areas, stained in uranyl acetate and lead citrate then viewed in a Phillips CM120 transmission electron microscope (FEI UK Ltd., Cambridge, England). Images were taken on a Gatan Orius CCD camera (Gatan UK, Oxon, England). Samples for SEM were gold sputter coated and viewed using a Hitachi S-2600N digital scanning electron microscope (Oxford Instruments, Oxfordshire, UK).

Statistical Analysis. All data are shown as the mean $\pm$ sem, and these were analyzed using one-way analysis of variance (ANOVA). Multiple comparison were analyzed using the Tukey-HSD method and in all cases, values of $P < 0.05$ were consider significant. (GraphPad InStat Software Inc., CA, USA).

Supporting Information Available: ICP–MS analysis of soluble metals in supernatant of CB and GP (Table 1); calculation of the aerodynamic diameter of nanoplatelet shaped particles; gross pathology of lung section after 24 h exposure, (Figure I); response to CB and GP treated mice after 1 week, including cell count and histology of lung and pleura (Figures II and III). This material is available free of charge *via* the Internet at http://pubs.acs.org.

REFERENCES AND NOTES

1. Novoselov, K. S.; Geim, A. K.; Morozov, S. V.; Jiang, D.; Zhang, Y.; Dubonos, S. V.; Grigorieva, I. V.; Firsov, A. A. Electric Field Effect in Atomically Thin Carbon Films. *Science* **2004**, *306*, 666–669.

2. Sanchez, V. C.; Jachak, A.; Hurt, R. H.; Kane, A. B. Biological Interactions of Graphene-Family Nanomaterials—An Interdisciplinary Review. *Chem. Res. Toxicol.* **2011**.

3. Jones, A. D.; Ellison, J. M. Respirable Industrial Fibres: Deposition, Clearence and Dissolution in Animal Models. *Ann Occup. Hyg.* **1993**, *37*, 211–226.

4. Donaldson, K. The Inhalation Toxicology of p-Aramid Fibrils. *Crit. Rev. Toxicol.* **2009**, *39*, 487–500.

5. Heintz, N. H.; Janssen-Heininger, Y. M.; Mossman, B. T. Asbestos, Lung Cancers, and Mesotheliomas: from Molecular Approaches to Targeting Tumor Survival Pathways. *Am. J. Respir. Cell Mol. Biol.* **2010**, *42*, 133–139.

6. Donaldson, K.; Murphy, F. A.; Duffin, R.; Poland, C. A. Asbestos, Carbon Nanotubes and The Pleural Mesothelium: A Review of the Hypothesis Regarding the Role of Long Fibre Retention in The Parietal Pleura, Inflammation and Mesothelioma. *Part Fibre. Toxicol.* **2010**, *7:5*, 5.

7. Murphy, F. A.; Poland, C. A.; Duffin, R.; Al-Jamal, K. T.; Ali-Boucetta, H; Nunes, A; Byrne, F; Prina-Mello; Volkov, Y; Li, S.; *et al.* Length-Dependent Retention of Carbon Nanotubes in the Pleural Space of Mice Initiates Sustained Inflammation and Progressive Fibrosis on The Parietal Pleura. *Am. J. Pathol.* **2011**, *178*, 2587–2600.

8. Miserocchi, G.; Sancini, G.; Mantegazza, F.; Chiappino, G. Translocation Pathways for Inhaled Asbestos Fibers. *Environ. Health.* **2008**, *7:4*, 4.

9. Ryman-Rasmussen, J. P.; Cesta, M. F.; Brody, A. R.; Shipley-Phillips, J. K.; Everitt, J. I.; Tewksbury, E. W.; Moss, O. R.; Wong, B. A.; Dodd, D. E.; Andersen, M. E.; *et al.* Inhaled Carbon Nanotubes Reach the Subpleural Tissue in Mice. *Nat. Nanotechnol.* **2009**, *4*, 747–751.

10. Mercer, R. R.; Hubbs, A. F.; Scabilloni, J. F.; Wang, L.; Battelli, L. A.; Schwegler-Berry, D.; Castranova, V.; Porter, D. W. Distribution and Persistence of Pleural Penetrations by Multiwalled Carbon Nanotubes. *Part Fibre. Toxicol.* **2010**, *7:28*, 28.

11. Muller, K. M.; Schmitz, I.; Konstantinidis, K. Black Spots of the Parietal Pleura: Morphology and Formal Pathogenesis. *Respiration* **2002**, *69*, 261–267.

12. Duch, M. C.; Budinger, G. R.; Liang, Y. T.; Soberanes, S.; Urich, D.; Chiarella, S. E.; Campochiaro, L. A.; Gonzalez, A.; Chandel, N. S.; Hersam, M. C.; *et al.* Minimizing Oxidation and Stable Nanoscale Dispersion Improves the Biocompatibility of Graphene in the Lung. *Nano Lett.* **2011**, *11*, 5201–5207.

13. Cho, W.-S.; Duffin, R.; Poland, C. A.; Howie, S. E.; MacNee, W.; Bradley, M.; Megson, I. L.; Donaldson, K. Metal Oxide Nanoparticles Induce Unique Inflammatory Footprints in The Lung: Important Implications for Nanoparticle Testing. *Environ. Health Perspect.* **2010**, *118*, 1699–1706.

14. Pumera, M. Electrochemistry Of Graphene: New Horizons for Sensing and Energy Storage. *Chem. Rec.* **2009**, *9*, 211–223.

15. Donaldson, K.; Tran, C. L. An Introduction to the Short-Term Toxicology of Respirable Industrial Fibres. *Mutat. Res.* **2004**, *553*, 5–9.

16. Donaldson, K.; Murphy, F.; Schinwald, A.; Duffin, R.; Poland, C. A. Identifying the Pulmonary Hazard of High Aspect Ratio Nanoparticles to Enable Their Safety-By-Design. *Nanomedicine. (London)* **2011**, *6*, 143–156.

17. Morgan, W. K. C.; Seaton, A. *Occupational Lung Disease*; 2nd ed.; WB Saunders Co.: Philadelphia, PA; 1984.

18. Cheng, Y.; Yeh, H.; Allen, M. D. Dynamic Shape Factor of a Plate-like Particle. *Aerosol Sci. Technol.* **1988**, *8*, 109–123.

19. Lordan, S.; Kennedy, J. E.; Higginbotham, C. L. Cytotoxic Effects Induced by Unmodified and Organically Modified Nanoclays in the Human Hepatic Hepg2 Cell Line. *J Appl. Toxicol.* **2011**, *31*, 27–35.

20. Porter, D. W.; Hubbs, A. F.; Mercer, R. R.; Wu, N.; Wolfarth, M. G.; Sriram, K.; Leonard, S.; Battelli, L.; Schwegler-Berry, D.; Friend, S.; *et al.* Mouse Pulmonary Dose- and Time Course-Responses Induced by Exposure to Multi-Walled Carbon Nanotubes. *Toxicology* **2010**, *269*, 136–147.

21. Poland, C. A.; Duffin, R.; Kinloch, I.; Maynard, A.; Wallace, W. A.; Seaton, A.; Stone, V.; Brown, S.; MacNee, W.; Donaldson, K. Carbon Nanotubes Introduced into the Abdominal Cavity of Mice Show Asbestos-like Pathogenicity in a Pilot Study. *Nat. Nanotechnol.* **2008**, *3*, 423–428.

22. Tatrai, E.; Brozik, M.; Kovacikova, Z.; Horvath, M. The Effect of Asbestos and Stone-Wool Fibres on some Chemokines and Redox System of Pulmonary Alveolar Macrophages and Pneumocytes Type II. *Biomed. Pap. Med. Fac. Univ. Palacky. Olomouc. Czech. Repub.* **2005**, *149*, 357–361.

23. Conti, P.; DiGioacchino, M. MCP-1 and RANTES are Mediators of Acute and Chronic Inflammation. *Allergy Asthma Proc.* **2001**, *22*, 133–137.

24. Gueugnon, F.; Leclercq, S.; Blanquart, C.; Sagan, C.; Cellerin, L.; Padieu, M.; Perigaud, C.; Scherpereel, A.; Gregoire, M. Identification of Novel Markers for the Diagnosis of Malignant Pleural Mesothelioma. *Am. J. Pathol.* **2011**, *178*, 1033–1042.

25. Palomaki, J.; Valimaki, E.; Sund, J.; Vippola, M.; Clausen, P. A.; Jensen, K. A.; Savolainen, K.; Matikainen, S.; Alenius, H. Long, Needle-like Carbon Nanotubes and Asbestos Activate the NLRP3 Inflammasome through a Similar Mechanism. *ACS Nano* **2011**, *5*, 6861–6870.

26. Shinohara, H. Distribution of Lymphatic Stomata on the Pleural Surface of the Thoracic Cavity and the Surface

27. Marco, A. J.; Domingo, M.; Ruberte, J.; Carretero, A.; Briones, V.; Dominguez, L. Lymphatic Drainage of Listeria Monocytogenes and Indian Ink Inoculated in the Peritoneal Cavity of the Mouse. *Lab. Anim.* **1992**, *26*, 200–205.

28. Brown, D. M.; Kinloch, I. A.; Bangert, U.; Windle, A. H.; Walter, D. M.; Walker, G. S.; Scotchford, C. A.; Donaldson, K.; Stone, V. An *In Vitro* Study of the Potential of Carbon Nanotubes and Nanofibers to Induce Inflammatory Mediators and Frustrated Phagocytosis. *Carbon* **2007**, *45*, 1743–1756.

29. Dogra, S.; Donaldson, K. Effect of Long and Short Fibre Amosite Asbestos on *in Vitro* TNF Production by Rat Alveolar Macrophages: The Modifying Effect of Lipopolysaccharide. *Ind. Health.* **1995**, *33*, 131–141.

30. Wu, G.; Fang, Y. Z.; Yang, S.; Lupton, J. R.; Turner, N. D. Glutathione Metabolism and Its Implications for Health. *J. Nutr.* **2004**, *134*, 489–492.

31. Kelly, F. J.; Blomberg, A.; Frew, A.; Holgate, S. T.; Sandstrom, T. Antioxidant Kinetics in Lung Lavage Fluid Following Exposure of Humans to Nitrogen Dioxide. *Am. J Respir. Crit. Care Med.* **1996**, *154*, 1700–1705.

32. Brown, D. M.; Beswick, P. H.; Bell, K. S.; Donaldson, K. Depletion of Glutathione and Ascorbate in Lung Lining Fluid by Respirable Fibres. *Ann. Occup. Hyg.* **2000**, *44*, 101–108.

33. Brown, D. M.; Beswick, P. H.; Donaldson, K. Induction of Nuclear Translocation of NF-Kappa B in Epithelial Cells by Respirable Mineral Fibres. *J Pathol.* **1999**, *189*, 258–264.

34. Rahman, I.; MacNee, W. Role of Transcription Factors in Inflammatory Lung Diseases. *Thorax.* **1998**, *53*, 601–612.

35. Duncan, K. E.; Ghio, A. J.; Dailey, L. A.; Bern, A. M.; Gibbs-Flournoy, E. A.; Padilla-Carlin, D. J.; Roggli, V. L.; Devlin, R. B. Effect of Size Fractionation on the Toxicity of Amosite and Libby Amphibole Asbestos. *Toxicol. Sci.* **2010**, *118*, 420–434.

36. Broser, M.; Zhang, Y.; Aston, C.; Harkin, T.; Rom, W. N. Elevated Interleukin-8 in the Alveolitis of Individuals with Asbestos Exposure. *Int. Arch. Occup. Environ. Health.* **1996**, *68*, 109–114.

37. Dostert, C.; Petrilli, V.; Van, B. R.; Steele, C.; Mossman, B. T.; Tschopp, J. Innate Immune Activation Through Nalp3 Inflammasome Sensing of Asbestos and Silica. *Science* **2008**, *320*, 674–677.

38. Hornung, V.; Bauernfeind, F.; Halle, A.; Samstad, E. O.; Kono, H.; Rock, K. L.; Fitzgerald, K. A.; Latz, E. Silica Crystals and Aluminum Salts Activate the NALP3 Inflammasome through Phagosomal Destabilization. *Nat. Immunol.* **2008**, *9*, 847–856.

39. O'Neill, L. A. Immunology. How Frustration Leads to Inflammation. *Science* **2008**, *320*, 619–620.

40. Tschopp, J.; Schroder, K. NLRP3 Inflammasome Activation: The Convergence of Multiple Signalling Pathways on ROS Production? *Nat. Rev. Immunol.* **2010**, *10*, 210–215.

41. Petrilli, V.; Papin, S.; Dostert, C.; Mayor, A.; Martinon, F.; Tschopp, J. Activation of The NALP3 Inflammasome Is Triggered by Low Intracellular Potassium Concentration. *Cell Death. Differ.* **2007**, *14*, 1583–1589.

42. Martinon, F. Signaling by ROS Drives Inflammasome Activation. *Eur. J. Immunol.* **2010**, *40*, 616–619.

43. Donaldson, K. The Inhalation Toxicology of *p*-Aramid Fibrils. *Crit Rev. Toxicol.* **2009**, *39*, 487–500.

44. Rao, G. V.; Tinkle, S.; Weissman, D. N.; Antonini, J. M.; Kashon, M. L.; Salmen, R.; Battelli, L. A.; Willard, P. A.; Hoover, M. D.; Hubbs, A. F. Efficacy of a Technique for Exposing the Mouse Lung to Particles Aspirated from the Pharynx. *J Toxicol. Environ. Health A.* **2003**, *66*, 1441–1452.

45. Park, E. K.; Jung, H. S.; Yang, H. I.; Yoo, M. C.; Kim, C.; Kim, K. S. Optimized THP-1 Differentiation Is Required for the Detection of Responses to Weak Stimuli. *Inflammation Res.* **2007**, *56*, 45–50.

Topography of the Pleural Mesothelium in the Golden Hamster. *Anat. Rec.* **1997**, *249*, 16–23.